Molecular Bandgap Engineering of Bottom-Up Synthesized Graphene Nanoribbon Heterojunctions

Yen-Chia Chen[1, 2], Ting Cao[1, 2], Chen Chen[3], Zahra Pedramrazi[1], Danny Haberer[1], Dimas G. de Oteyza[1, 4], Felix R. Fischer[2, 3, 5]*, Steven G. Louie[1, 2]*, and Michael F. Crommie[1, 2, 5]*

[1] Department of Physics, University of California at Berkeley, Berkeley, CA 94720, USA.

[2] Materials Sciences Division, Lawrence Berkeley National Laboratory, Berkeley, CA 94720, USA.

[3] Department of Chemistry, University of California at Berkeley, Berkeley, CA 94720, USA.

[4] Centro de Física de Materiales CSIC/UPV-EHU-Materials Physics Center, San Sebastián, E-20018, Spain.

[5] Kavli Energy NanoSciences Institute at the University of California Berkeley and the Lawrence Berkeley National Laboratory, Berkeley,CA 94720, USA.

Bandgap engineering plays a vital role in technology by enabling semiconductor heterostructures to perform important processes such as resonant tunneling[1,2] and efficient solar conversion.[3,4] As such devices reduce in size, however, their performance suffers.[5,6] Graphene-based molecular electronics has emerged as a candidate to enable high electronic performance down to single-molecule scales.[7-17] Graphene nanoribbons (GNRs), for example, can have widths < 2nm and bandgaps that are tunable via width and symmetry.[6,18,19] It has been predicted that bandgap engineering within single GNRs may be achieved by varying the width of covalently bonded GNR segments.[20-22] While partially cyclized GNRs made from a single precursor type have been synthesized,[9] so far there has been no experimental demonstration of GNR-based bandgap engineering or the use of multiple precursor types to create broader classes of width-modulated GNR heterojunctions. Here we demonstrate bottom-up synthesis of width-modulated armchair GNR heterostructures obtained by fusing segments made from two different molecular building blocks. We study these heterojunctions at sub-nanometer length-scales via scanning tunneling microscopy (STM) and spectroscopy (STS), and identify spatially modulated electronic structure demonstrating molecular-scale bandgap engineering, including type I heterojunction behavior. First-principles calculations support these findings and provide insight into the microscopic electronic structure of bandgap-engineered GNR heterojunctions.

Our GNR heterojunctions were fabricated by combining the molecular building blocks 10,10'-dibromo-9,9'-bianthracene (**1**) and 2,2'-di((1,1'-biphenyl)-2-yl)-10,10'-dibromo-9,9'-bianthracenethe (**2**). As depicted in Fig. 1A, molecules **1** and **2** are precursors to $N = 7$ and $N = 13$ armchair GNRs, respectively (referred to as 7-AGNRs and 13-AGNRs), where N is the width

in number of rows of carbon atoms across the GNR.[11,12] The building blocks were sublimed onto a Au(111) surface held at room temperature in ultrahigh vacuum (UHV). The surface was then heated to 470 K for 10 min to induce homolytic cleavage[23] of the labile C–Br bonds in the molecular building blocks **1** and **2**, yielding surface stabilized diradical intermediates. Since **1** and **2** share the same bianthracene backbone, their diradical intermediates are structurally complementary and are able to colligate into linear polymers. Upon further heating to 670 K for 10 min, a stepwise cyclization/dehydrogenation sequence converted these linear polymers into 7-13 GNR heterojunctions (Fig. 1).[11,12] The samples were then cooled down to 7 K for STM and STS measurements. Fig. 1B shows an STM topographic image of a representative sample, exhibiting 7-13 GNR heterojunctions whose shapes resemble the sketch in Fig. 1A. The narrower segments in these heterojunctions measure 1.3 ± 0.1 nm in width in the STM image, and are composed of covalently bonded monomers of **1** ($N = 7$). The wider segments measure 1.9 ± 0.2 nm in apparent width and consist of bonded monomers of **2** ($N = 13$). Since the building blocks mixed and fused in a random sequence during the initial step-growth polymerization, various $N = 7$ and $N = 13$ segment lengths were observed (see Fig. 1B inset).

To investigate the local electronic structure of these 7-13 GNR heterojunctions, tunneling conductance dI/dV spectra were recorded while placing the STM tip at different positions above the GNR heterojunctions (dI/dV magnitude reflects the energy-dependent local density of states (LDOS) at the STM tip position). As a background reference, a dI/dV spectrum taken on bare Au(111) is shown in green in Fig. 2. A characteristic spectrum (blue curve) recorded at the indicated position on an $N = 7$ segment of a single heterojunction (image shown in Fig. 2 inset) exhibits a pronounced shoulder at $V_s = 1.86 \pm 0.02$ V (labeled state 1) and a peak at $V_s = -0.90 \pm 0.02$ V (V_s refers to the sample voltage). In contrast, the marked $N = 13$ segment (red curve)

shows prominent peaks at $V_s = 1.45 \pm 0.02$ V (labeled state 2) and $V_s = -0.12 \pm 0.02$ V. The energy locations of these states are similar to the valence and conduction bandedges reported previously for isolated 7-AGNRs and 13-AGNRs on Au(111).[12,17] Additional states are observed in dI/dV spectra measured at positions near the interface between the $N = 7$ and $N = 13$ segments of a heterojunction. The black curve in Fig. 2, obtained at the interface position marked by the black cross in Fig. 2 inset, exhibits two additional overlapping peaks labeled state 3 and state 4 (other sets of data showing these peaks more clearly can be found in the SI). Lorentzian peak-fitting yields peak positions for states 3 and 4 of $V_s = 1.25 \pm 0.02$ V and $V_s = 1.13 \pm 0.02$ V, respectively. All of these spectroscopic features were consistently observed on all ten GNR heterojunctions whose nanoribbon segments and interfaces were inspected via dI/dV tunneling spectroscopy using different STM tips (all heterojunctions inspected via dI/dV had both $N = 7$ and $N = 13$ segments composed of at least two monomer units each; *i.e.*, segment lengths ≥ 1.6 nm).

The spatial distributions of GNR heterojunction states 1–4 were explored experimentally using dI/dV mapping (Figs. 3A–D). Fig. 3A shows the dI/dV map obtained for the highest-energy state (state 1) at $V_s = 1.86$ V for the same heterojunction shown in the inset to Fig. 2. The dI/dV map of state 1 exhibits significant LDOS at the edges of the narrower $N = 7$ segment, and some LDOS at the edges of the wider $N = 13$ segment. Fig. 3B shows the dI/dV map obtained at the energy of state 2 ($V_s = 1.45$ V). This lower-energy state shows significant LDOS near the edges of the wider $N = 13$ heterojunction segment, but no LDOS in the narrower $N = 7$ segment. Fig. 3C shows the dI/dV map of state 3 at $V_s = 1.25$ V. This even lower-energy state exhibits significant LDOS at the corners of the interface between the $N = 7$ and $N = 13$ segments, as well as some LDOS at the outer edges of the wider $N = 13$ segment. Fig. 3D shows the dI/dV map of

state 4, the lowest-energy peak for the unoccupied states, at $V_s = 1.15$ V. This state exhibits LDOS localized to the corners of the interface between the $N = 7$ and $N = 13$ regions, but very little LDOS anywhere else.

The overall electronic structure of 7-13 GNR heterojunctions shows some features that can be intuitively understood. For example, the fact that the highest-energy unoccupied state (#1) shows LDOS in both the narrower and the wider segments while the adjacent, lower-energy state (#2) shows significant LDOS only in the wider segment is consistent with a simple quantum well picture. Other features, however, are harder to understand. The origin of the interface states 3 and 4, for example, are not intuitive within the quantum well picture. Moreover, the fact that GNR heterojunctions exhibit high LDOS intensity at their edges but not in their interiors (similar to previously reported pristine 7- and 13-AGNRs[12,14,17,24]) conflicts with previous theoretical predictions that there are no localized edge-states in AGNRs near the bandedges.[18]

In order to answer these questions and to better understand the properties of 7-13 GNR heterojunctions, we used first-principles density functional theory (DFT) within the local density approximation (LDA) to calculate their electronic structure.[25] The simulation was based on the isolated 7-13 junction structure shown in the inset to Fig. 4A (all edges were terminated by hydrogen atoms, consistent with the experiment). The resulting density of states is plotted in Fig. 4A, with a Gaussian broadening of 0.06 eV (states localized at the two ends of the structure[18,26] were removed from the plot since we probed regions far from the ends of the GNR heterostructures (see Methods)). The four lowest unoccupied states are numbered 1–4 in descending order of energy, analogous to the labeling of the resonant states observed experimentally (Fig. 2). Out-of-plane height-integrated (h-integrated) LDOS plots (Figs. 4B–4E) provide detailed information regarding the averaged planar (x-y) spatial distribution of these four

calculated states. The lower-energy states 2, 3, and 4 are localized mainly on the wider $N = 13$ segment and can be understood as confined states in a potential well, with the adjacent and narrower $N = 7$ segments acting as energy barriers. The highest-energy state 1 extends over the entire heterojunction including both the wide $N = 13$ and narrow $N = 7$ segments. All four states show significant intensity in the interior of the heterojunction and there are no localized edge-states (as expected for armchair-edged GNR structures[18,19]). This appears to be in contradiction with the experimental dI/dV maps depicted in Figs. 3A–3D where only the edges exhibit LDOS noticeably higher than the background.

We are able to resolve this apparent contradiction by examining the height-dependence of the calculated 7-13 GNR heterojunction LDOS as opposed to the height-integrated quantities. This is shown by the simulated dI/dV maps depicted in Figs. 4G–4I, which illustrate the height-dependence of the LDOS for one particular state (#2) at different distances h above the GNR heterojunction. At a height of $h = 2$ Å above the carbon plane (Fig. 4G) the LDOS appears rather uniformly distributed across the $N = 13$ segment, resembling the height-integrated LDOS shown in Fig. 4C. However, as one moves higher above the carbon plane, the heterojunction edges begin to exhibit more intense LDOS than the interior (Figs. 4H and 4I), to the point where the edges completely dominate the LDOS at a height of $h = 4$ Å above the carbon plane (Fig. 4I). Simulated dI/dV maps at even higher distances appear similar to Fig. 4I. This type of behavior was observed for all four of the calculated quantum well states of the heterojunction. Since our STM tip is located approximately 5 Å above the carbon plane of the GNR heterojunctions during dI/dV mapping (estimated via the tunnel junction resistance at the open-feedback set points), the experimental dI/dV maps should be directly compared with the theoretical LDOS calculated in a plane *above* the heterojunction. Indeed, the calculated LDOS of heterojunction states 1–4 at a

height of 4 Å above the carbon plane (Figs. 3E–3H) match the corresponding experimental dI/dV maps very well (Figs. 3A–3D).

The strong dependence of the LDOS distribution with height h can be explained by the difference in potential energy felt by electrons at different (x, y) positions above a GNR heterojunction, as illustrated in Fig. 4F. The red curve in Fig. 4F shows the calculated potential energy difference (within LDA) between positions A_1 and A_2 in the $N = 7$ segment (marked in the inset structural drawing) as a function of height; A_1 marks a carbon atom at the very edge of the segment whereas A_2 marks an adjacent carbon atom just one dimer row into the interior. The potential energy at the edge is lower than the potential energy in the interior for heights greater than 1.6 Å above the GNR heterojunction. This implies a smaller out-of-plane (h direction) potential barrier in the vacuum for electrons closer to the edge. The wavefunction at the edge therefore decays along the h direction into the vacuum more slowly than the wavefunction in the interior, resulting in higher LDOS contrast between the edges and the interior as shown in Fig. 4I (see Fig. 4F inset sketch). The same argument also applies to the $N = 13$ segment (green curve in Fig. 4F). The stronger spectroscopic dI/dV signal observed near the edges of armchair GNRs is thus attributed to spatial variation in the electronic potential, even though the states themselves are not localized to the edges (additional discussion in SI).

These results imply that the band alignment in 7-13 GNR heterojunctions is very similar to type I semiconductor junctions since the lowest unoccupied (highest occupied) state in the $N = 13$ segment is lower (higher) than that in the $N = 7$ segment. The $N = 7$ segment might therefore serve as an energy barrier for charge carriers trapped in the $N = 13$ segment (our spectroscopic data implies that the energy required to excite an electron from state 4, which is localized in the $N = 13$ segment, to state 1 and thus into the $N = 7$ segment is ~0.7 eV). This provides a possible

means for constructing graphene quantum-dot-based systems with sub-nm feature sizes and single-atom thickness. A potential benefit of this heterojunction architecture is that electrical contacts to the quantum dots are readily available via the outer GNR segments. Bottom-up GNR-based synthesis methods thus have potential for creating functional gap-modulated semiconductor junctions with atomically-controlled features that are smaller than what is possible through conventional top-down lithography.

Methods

A polished Au(111) single crystal was used as the substrate in this work. Standard Ar$^+$ sputtering/annealing cycles were applied to prepare an atomically clean surface. The molecular building blocks **1** and **2** were loaded in different crucibles in a home-made double-crucible evaporator that allowed separate temperature control over each crucible. We sublimed **1** and **2** from crucibles held at 415 K and 490 K in UHV, respectively, onto Au(111) that was held at room temperature (depositions were monitored using a quartz crystal microbalance). We then heated the sample to 470 K first and then 670 K for 10 minutes each, which resulted in the molecular building blocks converting into 7-13 GNR heterojunctions.

STM measurements were performed using a home-built UHV low-temperature STM operated at 7 K. A Pt-Ir tip was used for topographic and spectroscopic measurements. For spectroscopic measurements dI/dV signals were recorded by a lock-in amplifier while the sample bias was modulated by a 451 Hz, 5–10 mV (r.m.s.) sinusoidal voltage under open-feedback conditions. WSxM was used to process all STM images.[27]

First-principles calculations of 7-13 GNR heterojunctions were performed using density functional theory in the local density approximation implemented in the Quantum Espresso package.[28] A supercell arrangement was used,[29] with the cell dimension carefully tested to avoid interactions between the heterojunction and its periodic image. We employed norm conserving pseudopotentials,[30] with a plane-wave energy cutoff of 60 Ry. The structure was fully relaxed until the force on each atom was smaller than 0.02 eV/Å. All the σ dangling bonds on the edge of the heterojunction were capped by hydrogen atoms. In the simulation of dI/dV spectra, a Gaussian broadening of 0.06 eV was used. The effect of substrate-screening on self-energy corrections was estimated using the GW technique for model systems (see S.I.).

Author contributions

Y.-C.C., C.C., Z.P., D.H., D.G.O. and M.F.C. performed STM measurements and analyzed STM data. T.C. and S.G.L. carried out GNR calculations and interpretation of STM data. F.R.F. synthesized the precursor molecules. All authors discussed and wrote the paper.

Additional information

Supplementary information is available in the online version of the paper. Reprints and permission information is available online at http://www.nature.com/reprints. Correspondence and requests for materials should be addressed to F.R.F. (ffischer@berkeley.edu), S.G.L. (sglouie@berkeley.edu) and M.F.C. (crommie@berkeley.edu).

Competing financial interests

The authors declare no competing financial interests.

References

1. Chang, L. L., Esaki, L. & Tsu, R. Resonant tunneling in semiconductor double barriers. *Appl. Phys. Lett.* **24**, 593 (1974).

2. Zwanenburg, F. A. *et al.* Silicon quantum electronics. *Rev. Mod. Phys.* **85**, 961–1019 (2013).

3. Green, M. A., Emery, K., Hishikawa, Y., Warta, W. & Dunlop, E. D. Solar cell efficiency tables (version 40). *Prog. Photovolt: Res. Appl.* **20**, 606–614 (2012).

4. Guter, W. *et al.* Current-matched triple-junction solar cell reaching 41.1% conversion efficiency under concentrated sunlight. *Appl. Phys. Lett.* **94**, 223504 (2009).

5. Frank, D. J. *et al.* Device scaling limits of Si MOSFETs and their application dependencies. *Proc. IEEE* **89**, 259–288 (2001).

6. Schwierz, F. Graphene transistors. *Nat. Nanotechnol.* **5**, 487–496 (2010).

7. van der Lit, J. *et al.* Suppression of electron-vibron coupling in graphene nanoribbons contacted via a single atom. *Nat. Commun.* **4**, 2023 (2013).

8. Bennett, P. B. *et al.* Bottom-up graphene nanoribbon field-effect transistors. *Appl. Phys. Lett.* **103**, 253114 (2013).

9. Blankenburg, S. *et al.* Intraribbon Heterojunction Formation in Ultranarrow Graphene Nanoribbons. *ACS Nano* **6**, 2020–2025 (2012).

10. Bronner, C. *et al.* Aligning the Band Gap of Graphene Nanoribbons by Monomer Doping. *Angew. Chem., Int. Ed.* **52**, 4422–4425 (2013).

11. Cai, J. *et al.* Atomically precise bottom-up fabrication of graphene nanoribbons. *Nature* **466**, 470–473 (2010).

12. Chen, Y.-C. *et al.* Tuning the Band Gap of Graphene Nanoribbons Synthesized from Molecular Precursors. *ACS Nano* **7**, 6123–6128 (2013).

13. Han, M., Özyilmaz, B., Zhang, Y. & Kim, P. Energy Band-Gap Engineering of Graphene Nanoribbons. *Phys. Rev. Lett.* **98**, 206805 (2007).

14. Koch, M., Ample, F., Joachim, C. & Grill, L. Voltage-dependent conductance of a single graphene nanoribbon. *Nat. Nanotechnol.* **7**, 713–717 (2012).

15. Li, X., Wang, X., Zhang, L., Lee, S. & Dai, H. Chemically Derived, Ultrasmooth Graphene Nanoribbon Semiconductors. *Science* **319**, 1229–1232 (2008).

16. Linden, S. *et al.* Electronic Structure of Spatially Aligned Graphene Nanoribbons on Au(788). *Phys. Rev. Lett.* **108**, 216801 (2012).

17. Ruffieux, P. *et al.* Electronic Structure of Atomically Precise Graphene Nanoribbons. *ACS Nano* **6**, 6930–6935 (2012).

18. Nakada, K., Fujita, M., Dresselhaus, G. & Dresselhaus, M. S. Edge state in graphene ribbons: Nanometer size effect and edge shape dependence. *Phys. Rev. B* **54**, 17954 (1996).

19. Son, Y.-W., Cohen, M. L. & Louie, S. G. Energy Gaps in Graphene Nanoribbons. *Phys. Rev. Lett.* **97**, 216803 (2006).

20. Prezzi, D., Varsano, D., Ruini, A. & Molinari, E. Quantum dot states and optical excitations of edge-modulated graphene nanoribbons. *Phys. Rev. B* **84**, 041401(R) (2011).

21. Sevinçli, H., Topsakal, M. & Ciraci, S. Superlattice structures of graphene-based armchair nanoribbons. *Phys. Rev. B* **78**, 245402 (2008).

22. Xu, Z., Zheng, Q.-S. & Chen, G. Elementary building blocks of graphene-nanoribbon-based electronic devices. *Appl. Phys. Lett.* **90**, 223115 (2007).

23. Franc, G. & Gourdon, A. Covalent networks through on-surface chemistry in ultra-high vacuum: state-of-the-art and recent developments. *Phys. Chem. Chem. Phys.* **13**, 14283–14292 (2011).

24. Ijäs, M. *et al.* Electronic states in finite graphene nanoribbons: Effect of charging and defects. *Phys. Rev. B* **88**, 075429 (2013).

25. LDA calculations generally underestimate energy gaps. Since the graphene nanoribbons were supported by a gold surface in the experiments, metallic screening of the substrate renormalizes the quasiparticle excitation energies, bringing them closer to those of the Kohn-Sham orbital energies of DFT (this statement is supported by additional model calculations discussed in the S.I.).

26. Hod, O., Peralta, J. & Scuseria, G. Edge effects in finite elongated graphene nanoribbons. *Phys. Rev. B* **76**, 233401 (2007).

27. Horcas, I. *et al.* WSXM: A software for scanning probe microscopy and a tool for nanotechnology. *Rev. Sci. Instrum.* **78**, 013705 (2007).

28. Giannozzi, P. *et al.* QUANTUM ESPRESSO: a modular and open-source software project for quantum simulations of materials. *J. Phys.: Condens. Matter* **21**, 395502 (2009).

29. Cohen, M. L., Schlüter, M., Chelikowsky, J. R. & Louie, S. G. Self-consistent pseudopotential method for localized configurations: Molecules. *Phys. Rev. B* **12**, 5575–5579 (1975).

30. Troullier, N. & Martins, J. L. Efficient pseudopotentials for plane-wave calculations. *Phys. Rev. B* **43**, 1993–2006 (1991).
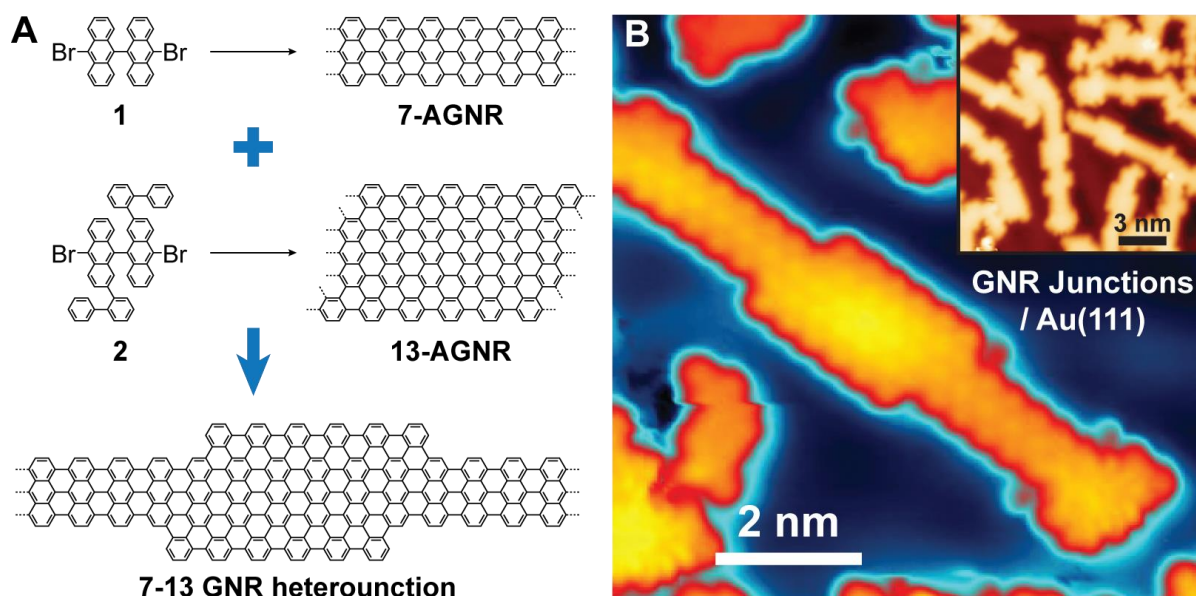
Figure 1. Bottom-up synthesis of 7-13 GNR heterojunctions. (A) Synthesis of 7-13 GNR heterojunctions from molecular building blocks **1** and **2**. The building blocks **1** and **2** are co-deposited onto a pristine Au(111) surface held at room temperature. Step-wise heating induces cleavage of the labile C–Br bonds, colligation (at 470 K), and then cyclization/dehydrogenation (at 670 K), resulting in 7-13 GNR heterojunctions. (B) High-resolution STM topograph of a 7-13 GNR heterojunction (V_s = 60 mV, I_t = 200 pA). Inset: larger-scale STM image of multiple GNR heterojunctions, showing a variety of segment lengths (V_s = 0.50 V, I_t = 2 pA).
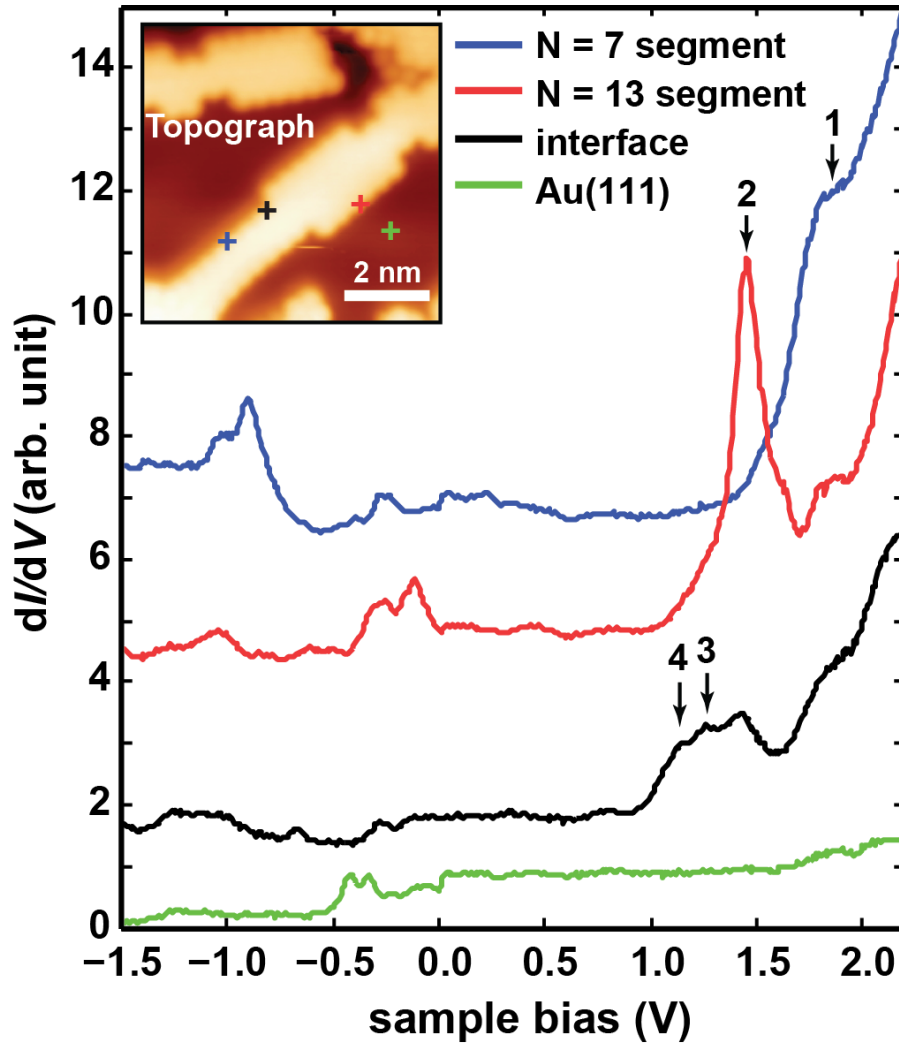
Figure 2. STM d*I*/d*V* spectroscopy of 7-13 GNR heterojunction electronic structure. Blue curve shows d*I*/d*V* spectrum acquired on the narrow $N = 7$ segment of a 7-13 GNR heterojunction (location of blue cross in inset). Red curve depicts spectrum acquired on wider $N = 13$ segment at location of red cross in inset. Black curve shows spectrum acquired at the interface region between $N = 7$ and $N = 13$ segments (location of black cross in inset). Green curve gives calibration spectrum acquired with tip held over bare Au(111) (all spectra shown here were acquired with the same STM tip). The black, red and blue curves are vertically offset by 1, 4 and

6 arbitrary units, respectively, for viewing clarity (open-feedback parameters: $V_s = 1.00$ V, $I_t =$ 35 pA; modulation voltage $V_{rms} = 10$ mV). Resonant peaks showing the locations of four GNR heterojunction states in the unoccupied region are labeled 1–4. Inset shows STM topograph of the 7-13 GNR heterojunction measured to obtain this series of dI/dV spectra ($V_s = 0.10$ V, $I_t = 95$ pA).
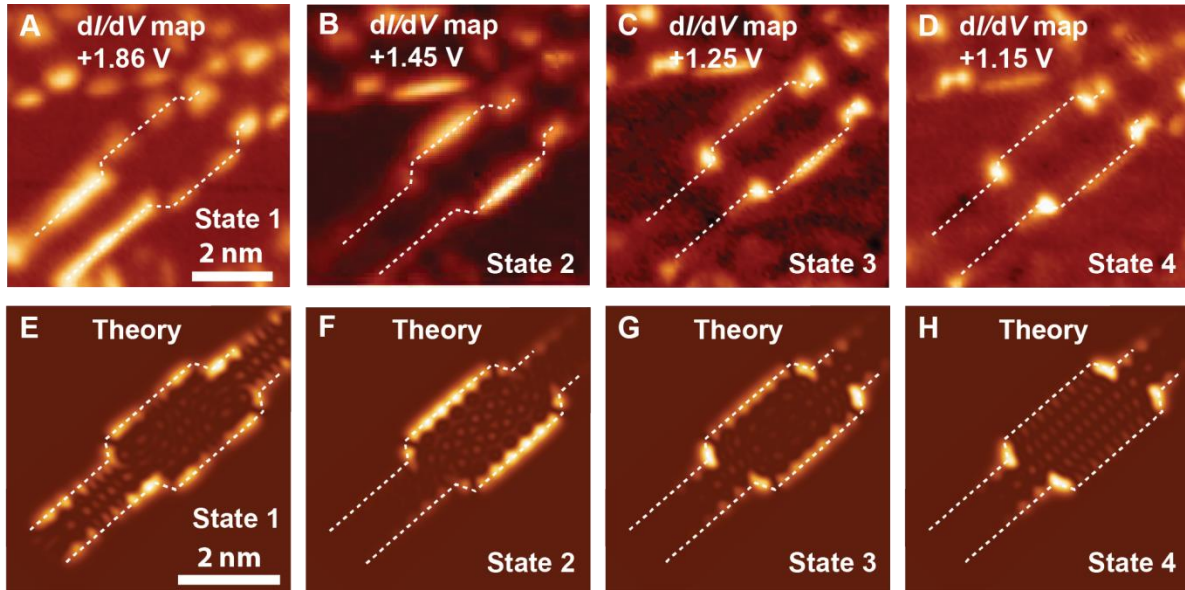
Figure 3. Comparison of experimental dI/dV maps and theoretical LDOS for a 7-13 GNR heterojunction. (A–D) Experimental dI/dV spatial maps recorded at energies of spectroscopic peaks 1–4 for the 7-13 GNR heterojunction shown in Fig. 2 inset (I_t = 35 pA; modulation voltage V_{rms} = 10 mV). The dashed lines are drawn at the mid-height topographic position of the edges for the 7-13 GNR heterojunction. (E–H) DFT calculated LDOS maps of states 1–4 calculated at a height of 4 Å above a 7-13 GNR heterojunction. The dashed lines here are drawn at a distance equal to one carbon dimer-dimer spacing (1.2 Å) outside of the 7-13 GNR heterojunction carbon atom border.
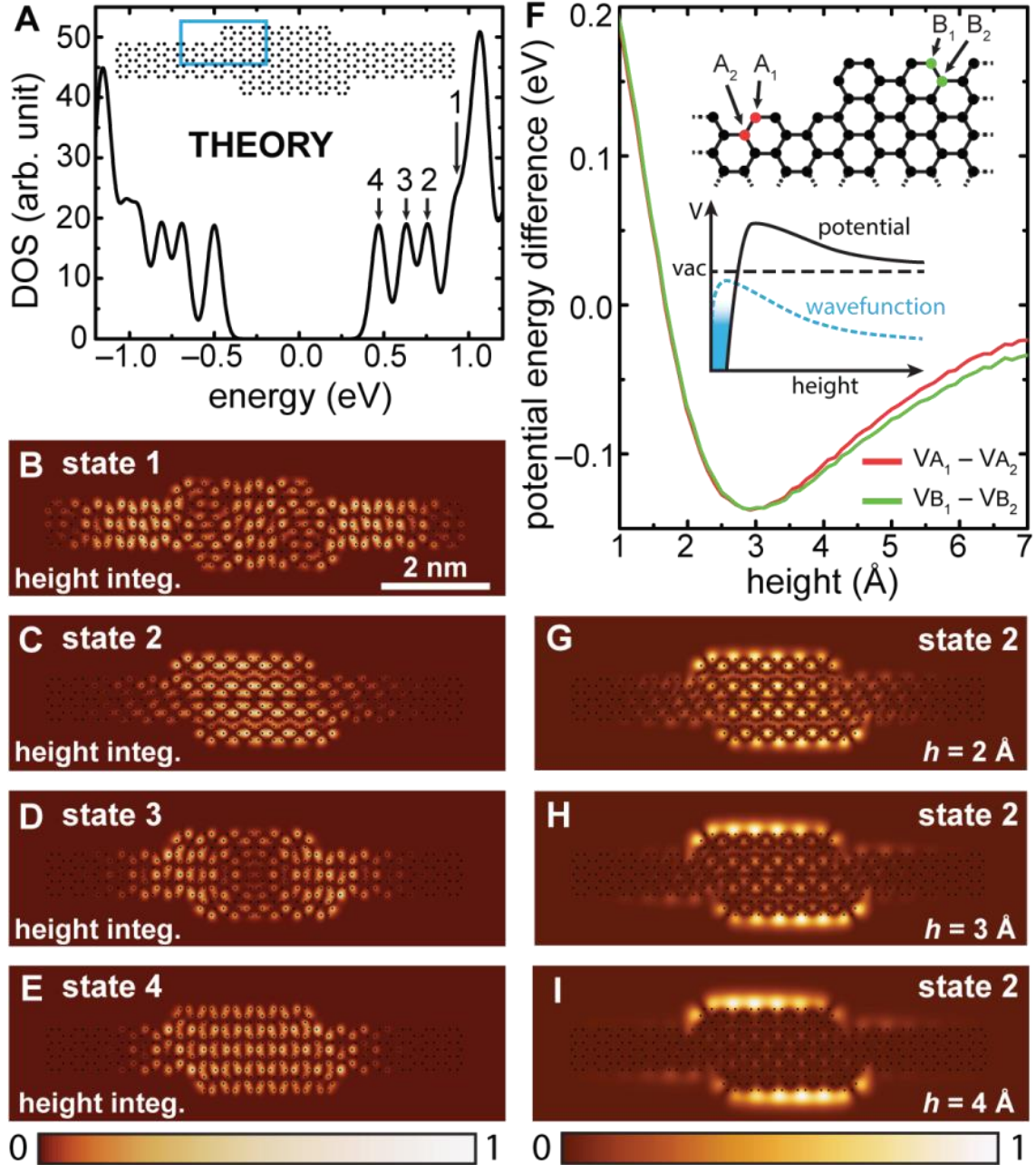
Figure 4. Theoretical electronic structure of 7-13 GNR heterojunction. (A) Calculated density of states of the isolated 7-13 GNR heterojunction structure shown in the inset, with a Gaussian broadening of 0.06 eV. Four unoccupied states are labeled 1–4 in the figure (states here are labeled analogous to the peaks observed experimentally (Fig. 2)). (B–E) Height-integrated

LDOS maps of theoretical states 1–4 for 7-13 GNR heterojunction. The plots are normalized with respect to their maximum intensities (270, 348, 500 and 416 arbitrary units in B–E, respectively). (F) Calculated electron potential energy difference between edge and inner atoms as a function of height h above the carbon plane of the 7-13 GNR heterojunction. The red (green) curve shows the potential energy difference between atomic positions A_1 and A_2 (B_1 and B_2) marked in the inset. The inset structural drawing depicts the boxed region in the inset to (A). The lower inset sketch represents the height dependence of the potential at one atomic location and the resulting decay of the wavefunction along the surface normal into the vacuum. The horizontal black dashed line indicates the vacuum energy level. (G–I) Calculated LDOS of 7-13 GNR heterojunction state 2 at heights of (G) 2 Å, (H) 3 Å, and (I) 4 Å above the plane of the GNR heterojunction. The LDOS plots are normalized with respect to their maximum intensities (180, 9.05 and 0.84 arbitrary units in G–I, respectively).